Cooper, C.M., Farrington, R.J., and Miller, M.S., 2020, On the destructive tendencies of cratons: Geology, v. 49, https://doi.org/10.1130/G48111.1

SUPPLEMENTAL MATERIAL

Cooper, Farrington, and Miller, 2020 – "*On the destructive tendencies of cratons"*

Methods:

Using the software package Underworld (Moresi et al. 2007), FEM integration is used to solve for the conservation of mass and momentum of an infinite Prandtl number, incompressible fluid defined, with variables from Table 1, as $v_{i,i} = 0$, $\tau_{ij,j} - p_i = f_i$, with v velocity, τ deviatoric stress, p pressure and f buoyancy force. A temperature and strain rate dependent dislocation and diffusion creep viscosity is used to define the constitutive relationship between stress and strain rate, defined as, $\eta_{\frac{diff}{disl}} = A^{-\frac{1}{n}} \exp\left(\frac{E+PV}{nRT_m}\right) \dot{\epsilon}_{II}^{\frac{1-n}{n}}$ with the variables defined in Supplementary Table S1 equivalent to dry olivine values from (Karato and Wu 1993) and (Hirth and Kohlstedt 2003). The harmonic mean of the diffusion and dislocation creep shear viscosity is calculated, and a maximum / minimum viscosity value of 10^{24} and 10^{19} is used. The prescribed initial thermal field is shown in Supplementary Figure S2.

We modeled a parameterized tectonic setting inspired by a subduction slab striking perpendicular to the continental lithosphere, which contains a craton south of the plate boundary. We used a 3D Cartesian model domain of length 5000 km, width 3000 km and height 660 km, with a grid resolution of 8 km / element in the horizontal and 5 km / element vertical. The craton region within the model spanned the southwestern region of the domain with dimensions 4000 (length) x 1400 (width) x 330 (depth, defined by the 1400 K isotherm) km with a northern margin width of 600 km and variable depths depending on chosen margin geometry. The slab, spanning 1000 km, representing the subducting oceanic lithosphere, with a thickness of 100 km, extends at a 60^o dip angle to the west into the mantle until it reaches a depth of 495 km.

The temperature field for the craton, margin, slab and mantle, shown in Fig. S2, are defined by inverting the half-space cooling model (Turcotte and Schubert 2014) for the parameterized cratonic, oceanic plate and subducting slab thickness at 1400 K, approximating the base of the lithosphere, shown in Figure 3(c), and parameters given in Table S1. The diagonal cratonic margin is defined by linearizing the calculated parameterized age between the thick craton (d3) and the oceanic plate across the margin.

We conducted a series of instantaneous flow models for four different cratonic margins with the same material properties and boundary conditions, including models with and without the subducting plate, outlined in Table S2. The instantaneous flow models provide a velocity and pressure field solution within the model domain from the prescribed initial temperature field, velocity boundary conditions and material constitutive relationships. The initial temperature field and constitutive relationships, accounting for both dislocation and diffusion creep, result in (i) the thermally driven sinking rigid slab and (ii) the mechanically strong cold, rigid cratonic interior. The instantaneous velocity solution, while not advected through a series of time steps, allows for the calculation of strain rate, and other time-dependent variables. We chose instantaneous flow models to isolate the complex flow fields produced by low driven by the subducting slabs interaction with cratonic lithosphere of varying

geometry. The models presented here demonstrate that the shape of cratons plays a significant role in this flow interaction indicating future development with 3D time-dependent models is worth pursuing.

We chose four different geometries of cratonic margins (Fig. 2 & S1 - tiered, diagonal, straight directly proximal to the subducting slab ("straight proximal"), and straight 300 km south of the slab ("straight distal")) to test whether the shape of the margin influenced the flow pattern and/or the potential for deformation. The tiered margin was modeled after the lithospheric thickness model, LITHO1.0 (Pasyanos et al. 2014) for the northern margin of South America with two steps of increasing lithospheric thickness. The first step spanned 300 km in width with a thickness of 66 km. The second step was also 300 km wide, but with a thickness of 198 km. We also tested a diagonal geometry with a slope defined by the linear transition from the thick cratonic to thin oceanic lithosphere to mimic the often observed and conceptualized craton margin as well as straight vertical margins similar to those observed in other cratons (e.g., (Bao, Eaton, and Guest 2014); Foster et al., 2014).

These shapes were roughly inspired by the tectonic settings of the westernmost Mediterranean and northeastern South America. In the westernmost Mediterranean, the subducted slab beneath the Gibraltar arc is dipping eastward and lies directly north of the West African craton (Bezada et al. 2013). The continental lithosphere has variable thickness (Fig. 1c), thinnest beneath the Atlas Mountains (~65 km), but then thickens south-eastward into the craton interior, gradually deepening (to ~220 km) (e.g. (Fishwick 2010; Cooper and Miller 2014; Meghan S. Miller et al. 2015b). Beneath northeastern South America (Fig. 1b), the lithosphere also has variable thickness (Meghan S. Miller et al. 2009; Feng, van der Lee, and Assumpção 2007; Heintz, Debayle, and Vauchez 2005; Masy et al. 2015) with the thickest lithosphere (>200 km) within the interior of the Amazonian craton, with steps in thickness, where the thinnest portion (<100 km) is located near the plate boundary (Levander et al., 2014). The continent is bounded by the oceanic Caribbean plate to the north beneath which the subducted Atlantic lithosphere dips westward (Bezada, Levander, and Schmandt 2010).

In our models mantle flow is driven by: (i) the negative thermal buoyancy of the slab (toroidal flow), and (ii) the thermal boundary layer between craton and mantle (edge-driven convection). These two processes are shown in isolation in (i) Fig. 2(a,b), and (ii) Fig. 2(c,d). The subduction induced mantle flow modelled here is produced by both the negative thermal buoyancy of the slab and the rigid plate strength. It is the combination of vertical sinking (buoyancy) and horizontal motion (strength) that produces the largely horizontal (lateral) mantle flow while the rigid slab sinks at an angle within the mantle. Subduction induced mantle flow can generally be partitioned into toroidal (horizontal circular ring) and poloidal (vertical circular ring) components. The toroidal flow dominance seen in our model is a result of the 60^{o} slab dip angle, slab width and mantle depth. The edge-driven convection is caused by the lateral temperature variations here introduced by the cratonic lithosphere producing small-scale convection with mantle velocities much smaller than those driven by the subducting slab.

Free-slip (mirror) velocity boundary conditions were used on all sides. Tracer particles are placed within the model domain along a North-South transect at a depth of 198 km directly to the west of the subducting slab. These particles are used to interpolate the strain rate values for locations shown in Fig. 3.

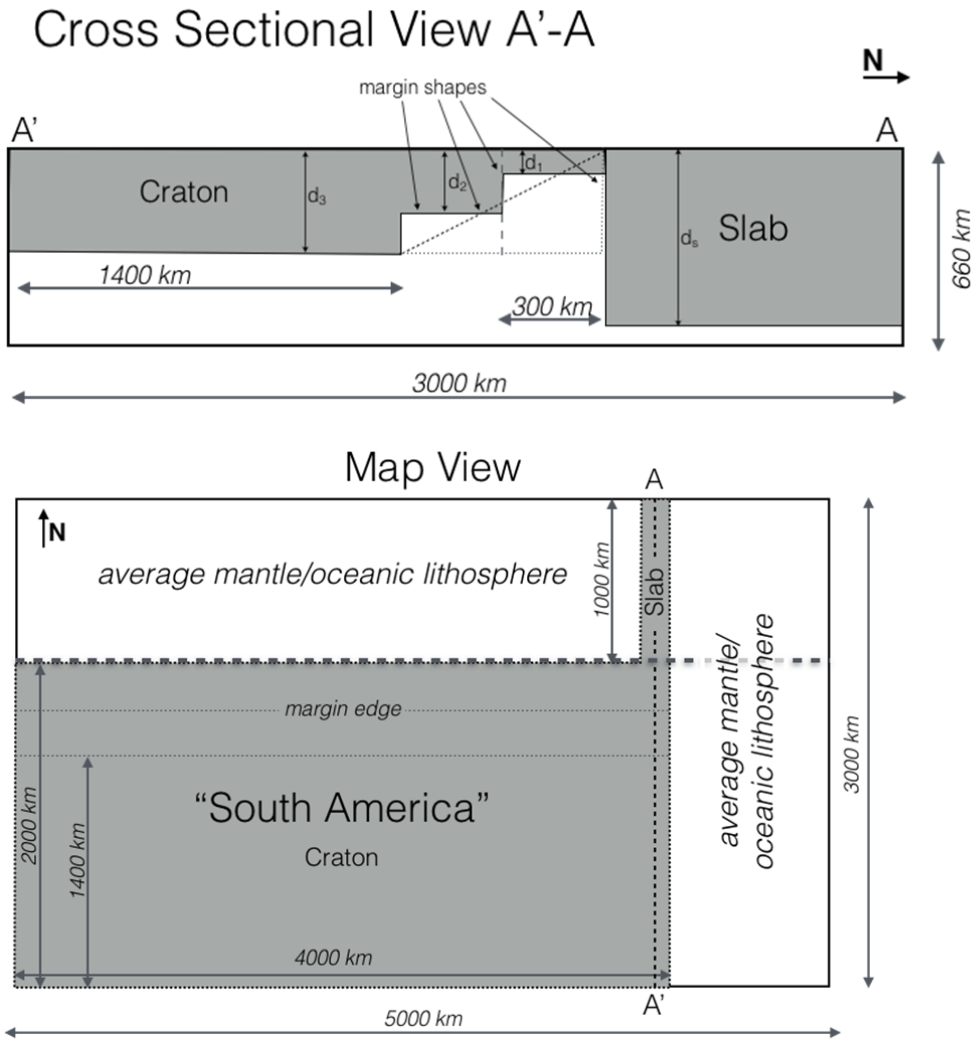

Figure S1. *Map view and cross section cartoon sketch of model geometry (not to scale) showing the different craton margins used within the simulations, (a) Cross Sectional View - 1) a tiered margin with two steps (solid black line), 2) a diagonal margin (dashed black line), 3) a straight vertical margin directly proximal to the slab (gray dotted line), and 4) a straight vertical margin 300 km from the slab (gray dashed line). The slab is 100km thick and extends to a depth of 495 km (d_s). The thickest craton region, d_3, is 330 km thick. The thickness of the two steps within the tiered craton geometry are 198 km (d_2) and 66 km (d_1). The steps are each 300 km wide. The "average mantle/oceanic lithosphere" region is represented with a 50 km oceanic lithosphere. The initial temperature field with depth for all regions is outlined in Supplementary Figure S2. Note, temperature structure of each craton shape has a slight curve shape due to the nonlinear nature of the half-space cooling model. (b) Map View. The dark gray, bold dashed line spanning the E-W length of the model demarcates the North-South regions used in the dissipation calculations (Supplementary Table S2 & S3). The region below this line is referred to as the "southern region" and encompasses the entire craton as well as the channel between the craton and the subducting slab.*

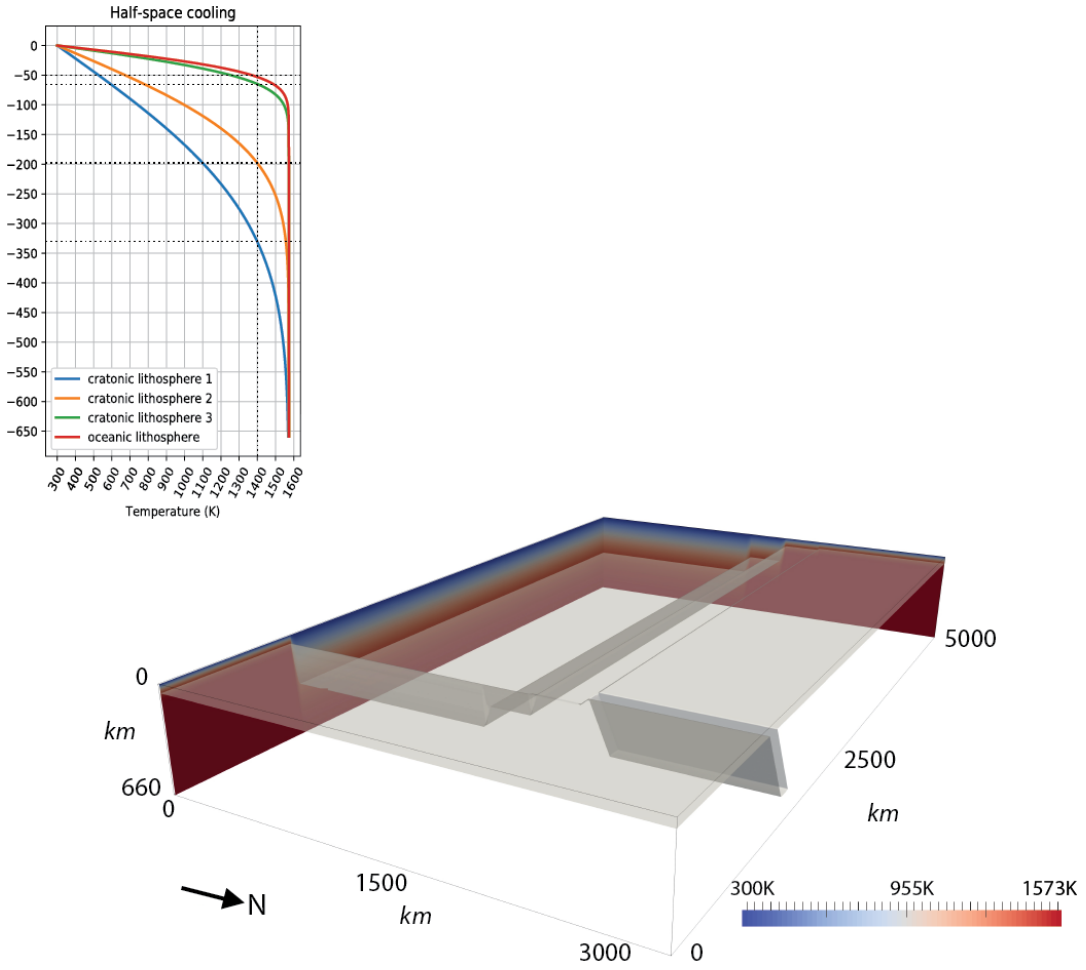

Figure S2. (a) *Half space cooling model used to prescribe temperature for the craton (craton 1 in inset), margin (craton 2 & 3 in inset), slab (at 60^{o} dip angle), oceanic lithosphere and mantle. Inverting the half-space cooling model for a prescribed lithospheric thickness, defined by the 1400 K isotherm, the following age-thickness values were used: cratonic lithosphere 1 (blue) 780 Ma - 330 k, cratonic lithosphere 2 (orange) 280 Ma -198 km, cratonic lithosphere 3 (green- 30 Ma -66 km, oceanic lithosphere (red) 20 Ma - 50 km. The subducting slab is 100 km thick (half space cooling age of 20 Ma about a symmetric plane extending from the midplane of the slab). Note, these ages do not represent the ages in northeastern South America, rather they are parameterized for the desired model thermal and rheological structure. (b) Initial temperature field in K within the craton (cold, blue), tiered margin, and the mantle (hot, red). Isosurface at 1400 K, approximating the base of the lithosphere (Turcotte and Schubert 2014).*

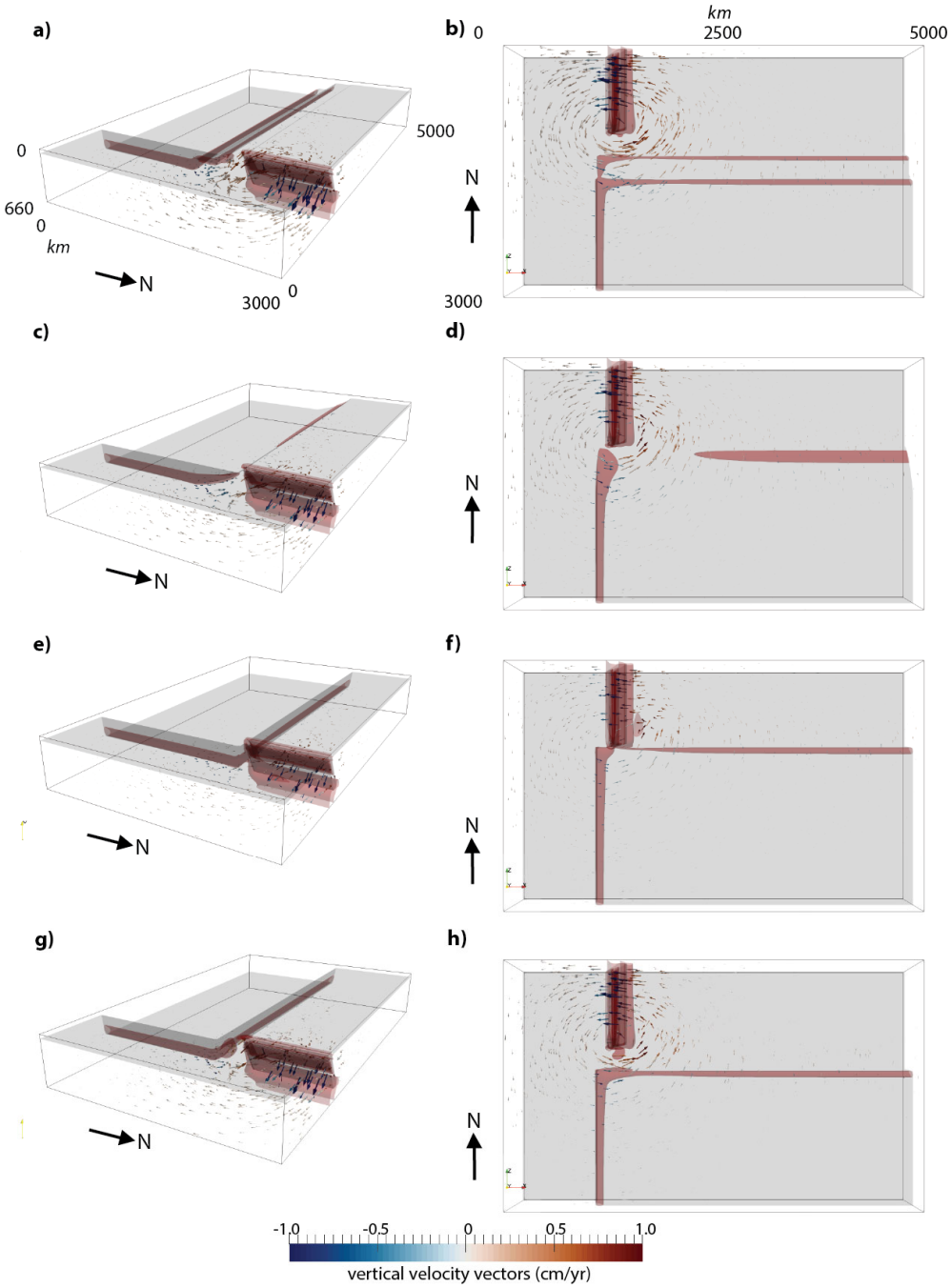

Figure S3*. Mantle flow (vectors) with temperature (grey) and dissipation (red) contours for (a,b) tiered craton plus slab model, (c,d) diagonal craton plus slab model (e,f) straight proximal craton and slab model, (g,h) and straight distal craton plus slab model. The panels on the right are a "devil's-eye view" from the base of the model and the panels on the left are viewed from the north-east. We use the "devil's eye view" to better visualize flow along the complex craton margin that might be masked by looking from above. Temperature contour at 1400 K, approximating the base of the lithosphere, velocity vectors colored by vertical velocity (Vy) as in Figure 2, dissipation contour at* 2×10^{-9} *Pa/s. The maximum velocity vector length scales to 5.6 cm/yr.*

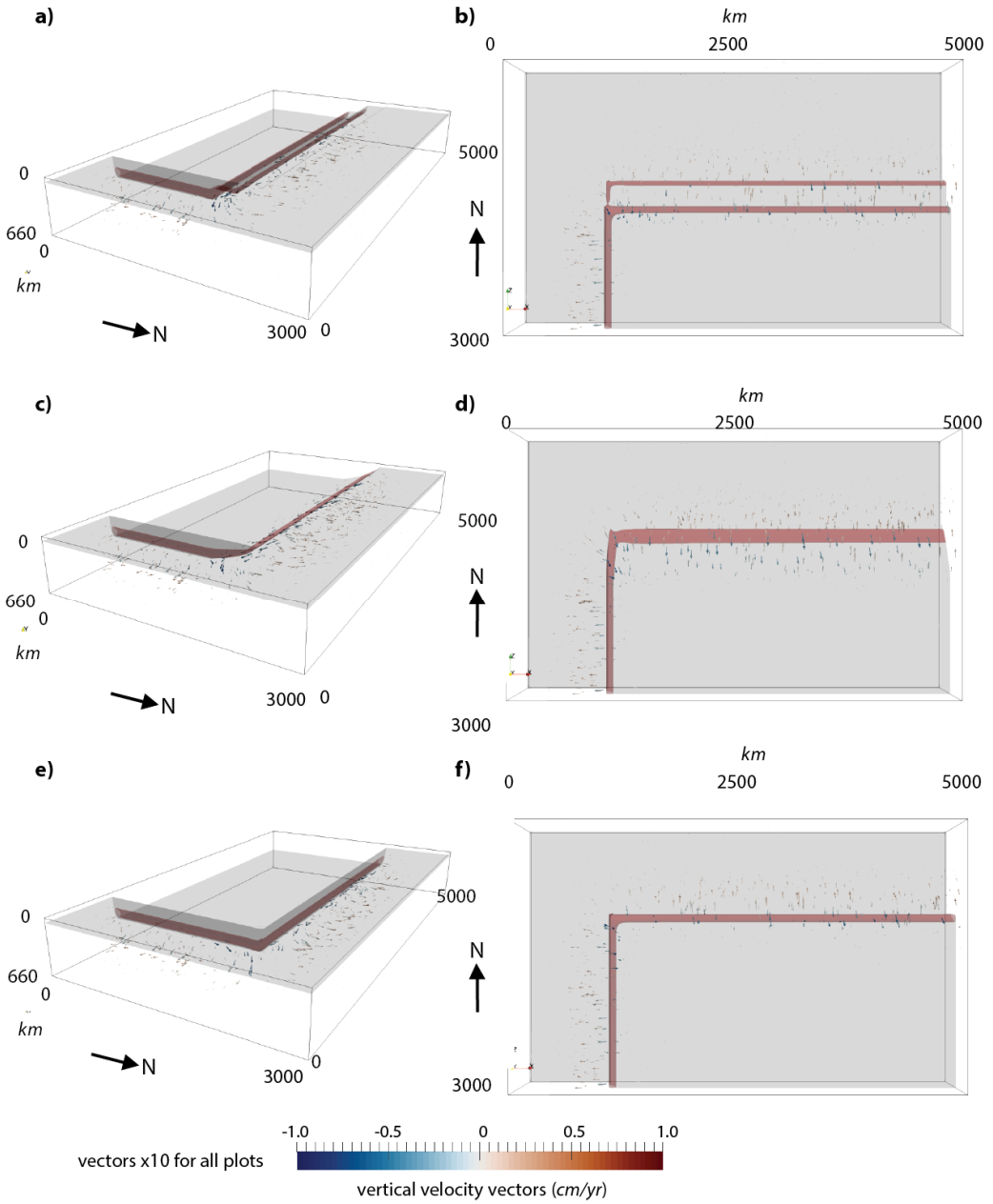

Figure S4. *Mantle flow (vectors) with temperature (grey) and dissipation (red) contours for (a,b) tiered craton model, (c,d) diagonal craton model, and (e,f) straight proximal craton model. The panels on the right are a "devil's-eye view" from the base of the model and the panels on the left are viewed from the north-east. We use the "devil's eye view" to better visualize flow along the complex craton margin that might be masked by looking from above. Temperature contour at 1400 K, approximating the base of the lithosphere, velocity vectors colored by vertical velocity (Vy) as in Figure 2, dissipation contour at* $2x10^{-9}$ *Pa/s. The maximum velocity vector length scales to 0.56 cm/yr. The largest velocity magnitude is associated with the corner of the craton; thermal downwellings within the mantle are concentrated at the location of thermal discontinuities, in particular, at discontinuities in both lateral directions (i.e. the third dimension, e.g., as shown in (Farrington et al. 2010)).*

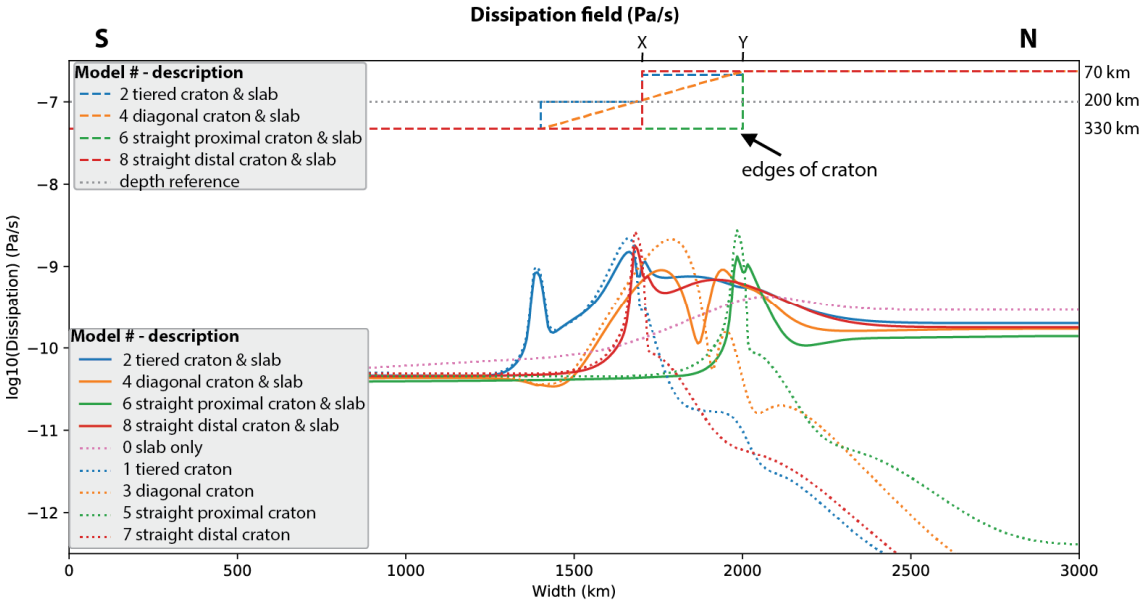

Figure S5. *Dissipation (Pa/s) along the North-South (labeled as N and S) transect shown with blue tracers in (Figure 3c) sampled at a depth of 198 km and directly to the west of the subducting slab as viewed from the "North". The transect runs parallel to the strike of the subducting slab and samples regions within the mantle wedge and extending into the cratonic lithosphere which is shown by the grey dotted lines in the top frame. Solid lines show values for the slab and craton models, dotted line for craton-only models, and the dashed lines in the top frame of the figure show the position and geometrically prescribed shape of the craton for reference. Note, the isotherms associated with the temperature structure of each craton shape will have a slight curved shape due to the nonlinear nature of the half-space cooling model. Tick marks labelled X on the horizontal axis identify the position of the edge of the craton for the straight distal craton (models 7 and 8). Tick marks labelled Y on the horizontal axis identify the position of the edge of the craton for the straight proximal craton (models 5 and 6). The X marks where the transect enters the diagonal margin craton (models 3 and 4) as well as where the transect runs along the base of the tiered margin craton (models 1 and 2). The transect intersects the deepest portion of the tiered margin craton at 1400 km (measured from the southern end). Numbering of the models follows the convention in Table S2.*

Table S1. *Model parameters and variable definitions used to model the craton, slab, and mantle.*

Variable	Symbol	Equation	Value	Units
gravity	*g*		9.8	$m.s^{-2}$
Thermal expansivity	α		3×10^{-5}	K^{-1}
Thermal diffusivity	κ		10^{-6}	$m^2.s^{-1}$
Reference density	ρ_0		3.3×10^3	$kg.m^{-3}$
Temperature	T			K
Temperature difference	ΔT	$T_{bot} - T_{top}$	1573 - 300 = 1273	K
Depth	*h*			m
Shear viscosity	η			Pa.s
Strain rate invariant	$\dot{\epsilon}_{II}$			s^{-1}
Shear stress	τ	$\eta\dot{\epsilon}$		Pa
Lithospheric Pressure	*P*	$\rho_0 gh$		Pa
Gas constant	*R*		8.3145	$J.K^{-1}.mol^{-1}$
Adiabatic mantle temperature	T_m	$T + 0.5h/1e3$		K
Prefactor, diffusion / dislocation	A		4×10^{-10} / 1×10^{-15}	$Pa^{-n}.s^{-1}$
Activation Energy, diffusion / dislocation	E		300×10^3 / 540×10^3	$J.mol^{-1}$
Activation Volume,diffusion / dislocation	V		4.5×10^{-6} / 10^{-5}	$m^3.mol^{-1}$
Stress exponent, diffusion / dislocation	n		1.0 / 3.5	-
Maximum shear viscosity	η_{max}		10^{24}	Pa.s
Minimum shear viscosity	η_{min}		10^{19}	Pa.s

Table S2. *Total energy dissipation within the total domain, southern, and northern regions in Watts. The regions are defined by the z plane running E-W, located adjacent to the southernmost edge of the slab, dividing the entire domain into a northern region (containing everything to the north of the southernmost edge of the subducting slab) and southern region (containing the craton as well as the channel, if present, between the craton and the subducting slab). The viscous dissipation per volume, defined as* $\dot{E} = \tau_{ij} \cdot \dot{\epsilon}_{II}$*, is the energy transferred to the volume by kinetic energy, the mantle flow. The effect of the slab on the craton can be determined by comparison between models with and without a subducting slab. The integrated dissipation per unit volume is the power dissipated in units of Watts, the energy dissipated per second.*

Model number	Name	Total	Southern Region (containing the craton and channel)	Northern Region (containing the slab)
0	Subducting slab only	1.776e+9	2.119e+8	1.564e+9
1	Tiered craton-only	7.221e+8	6.967e+8	2.543e+7
2	Tiered craton and slab	2.172e+9	9.620e+8	1.210e+9
3	Diagonal craton-only	7.689e+8	7.148e+8	5.414e+7
4	Diagonal craton and slab	2.078e+9	9.667e+8	1.111e+9
5	Straight Proximal craton-only	8.046e+8	7.019e+8	1.028e+8
6	Straight Proximal craton and slab	1.892e+9	8.790e+8	1.013e+9
7	Straight Distal craton-only	7.396e+8	7.070e+8	3.256e+7
8	Straight Distal craton and slab	2.085e+9	9.663e+8	1.119e+9

Dissipation

The percentage difference in dissipation between the craton and slab model, and craton-only model is shown in Table S3 for both the total domain and the southern region. The southern region contains everything to the south of the southernmost edge of the subducting slab (Figure S1), this includes the entirety of the craton as well as the channel, if present, along the craton margin between the craton and subducting slab.

Table S3. *Percentage difference of dissipation between the craton and slab, and craton-only models for the entire model domain and the southern region containing the craton and channel along the margin. The cross-section area of the channel is the region between the margin of the craton and the southern edge of the subducting slab along a plane in the N-S direction that parallels the westernmost edge of the craton (shapes visualized as the dashed lines in Figure 3).*

	Tiered	Diagonal	Straight Proximal	Straight Distal
Total domain	300%	270%	235%	282%
Southern region containing channel and craton	138%	135%	125%	137%
Cross-section area of channel	119×10^3 km^2	84×10^3 km^2	0 km^2	84×10^3 km^2

The subducting slab increases the amount of dissipation in the total domain of all models though the amount depends on the margin shape with the tiered margin showing the largest change and the straight, proximal margin the least. The trend also holds within the southern region suggesting that the amount of increase in dissipation corresponds with the size of the channel between the craton and the subducting slab where the “stirred” mantle flowed. Larger channels, such as for the tiered margin shape, allowed greater volume of flowing mantle to pass along the craton margin, causing a larger increase in dissipation. This is apparent when comparing the two models with the straight-shaped margins at differing distances from the subducting slab. The model with the straight proximal margin that abutted directly against the subducting slab, with the smallest channel cross-section area, resulted in the smallest increase in dissipation. In comparison, the straight distal model, which had the same margin shape, but a larger channel cross-section area, produced a greater increase in viscous dissipation. This demonstrates that the cross-sectional area of the channel, which can be controlled by margin shape or location relative to the subducting slab, influences the amount of channelization.

The presence of the subducting slab (solid lines in Supplementary Figure S5) increased dissipation within the mantle wedge (spanning 1700-2000 km on Supplementary Figure S5. For simulations with channels, the transects also show the increase in dissipation within the channel region (spanning between “X” & “Y”), where the stirred mantle is flowing along the margin, as shown in the calculations in Supplementary Table S3. Dissipation sharply increases at the craton boundary for all simulations and then decreases as the transect moves into the craton interior.

Data and materials availability: Figure 1 was created using data accessed November 2017 from http://www-udc.ig.utexas.edu/external/becker/ftp/jsg_geodynamics.sks.avg.table with details found here: http://www-udc.ig.utexas.edu/external/becker/sksdata.html. The following figures and tables - Figures 2, 3, Supplementary Figures S2, S3, Table 1, and Supplementary Table S2 - were made using model output. Details about the model including input and analysis scripts can be found here - https://github.com/RebeccaFarrington/cooper_destroyingcratons_2019. We used Underworld, an open-source code, (www.underworldproject.org) for the simulations in this work, version 2.5.0b. Python notebooks including analysis scripts, can be found here - https://github.com/RebeccaFarrington/cooper_destroyingcratons_2019.

Supplemental Material References:

Bao, Xuewei, David W. Eaton, and Bernard Guest. 2014. "Plateau Uplift in Western Canada Caused by Lithospheric Delamination along a Craton Edge." *Nature Geoscience* 7 (11): 830–33.

Bezada, M. J., E. D. Humphreys, D. R. Toomey, M. Harnafi, J. M. Dávila, and J. Gallart. 2013. "Evidence for Slab Rollback in Westernmost Mediterranean from Improved Upper Mantle Imaging." *Earth and Planetary Science Letters*. https://doi.org/10.1016/j.epsl.2013.02.024.

Bezada, M. J., A. Levander, and B. Schmandt. 2010. "Subduction in the Southern Caribbean: Images from Finite-Frequency P Wave Tomography." *Journal of Geophysical Research*. https://doi.org/10.1029/2010jb007682.

Cooper, C. M., and M. S. Miller. 2014. "Craton Formation: Internal Structure Inherited from Closing of the Early Oceans." *Lithosphere*. https://doi.org/10.1130/l321.1.

Farrington, R. J., Stegman, D. R., Moresi, L. N., Sandiford, M., & May, D. A. 2010. Interactions of 3D mantle flow and continental lithosphere near passive margins. *Tectonophysics*, *483*(1-2), 20-28.

Fishwick, S. 2010. "Surface Wave Tomography: Imaging of the Lithosphere–asthenosphere Boundary beneath Central and Southern Africa?" *Lithos*. https://doi.org/10.1016/j.lithos.2010.05.011.

Feng, Mei, Suzan van der Lee, and Marcelo Assumpção. 2007. "Upper Mantle Structure of South America from Joint Inversion of Waveforms and Fundamental Mode Group Velocities of Rayleigh Waves." *Journal of Geophysical Research, [Solid Earth]* 112 (B4). https://doi.org/10.1029/2006jb004449.

Foster, K., K. Dueker, B. Schmandt, and H. Yuan. 2014. "A Sharp Cratonic Lithosphere–asthenosphere Boundary beneath the American Midwest and Its Relation to Mantle Flow." *Earth and Planetary Science Letters* 402: 82–89.

Heintz, Maggy, Eric Debayle, and Alain Vauchez. 2005. "Upper Mantle Structure of the South American Continent and Neighboring Oceans from Surface Wave Tomography." *Tectonophysics* 406 (1-2): 115–39.

Hirth, Greg, and David Kohlstedt. 2003. "Rheology of the Upper Mantle and the Mantle Wedge: A View from the Experimentalists." In *Inside the Subduction Factory*, edited by John Eiler, 138:83–105. Geophysical Monograph Series. Washington, D. C.: American Geophysical Union.

Karato, S., and P. Wu. 1993. "Rheology of the Upper Mantle: A Synthesis." *Science* 260 (5109): 771–78.

Levander, A., Bezada, M.J., Niu, F., Humphreys, E.D., Palomeras, I., Thurner, S.M., Masy,

J., Schmitz, M., Gallart, J., Carbonell, R. and Miller, M.S., 2014. Subduction-driven recycling of continental margin lithosphere. *Nature*, 515(7526), pp.253-256.

Masy, Jeniffer, Fenglin Niu, Alan Levander, and Michael Schmitz. 2015. “Lithospheric Expression of Cenozoic Subduction, Mesozoic Rifting and the Precambrian Shield in Venezuela.” *Earth and Planetary Science Letters* 410: 12–24.

Moresi, L., S. Quenette, V. Lemiale, C. Mériaux, B. Appelbe, and H. -B. Mühlhaus. 2007. “Computational Approaches to Studying Non-Linear Dynamics of the Crust and Mantle.” *Physics of the Earth and Planetary Interiors* 163 (1-4): 69–82.

Miller, Meghan S., Leland J. O’Driscoll, Amber J. Butcher, and Christine Thomas. 2015. “Imaging Canary Island Hotspot Material beneath the Lithosphere of Morocco and Southern Spain.” *Earth and Planetary Science Letters* https://doi.org/10.1016/j.epsl.2015.09.026.

Miller, Meghan S., Alan Levander, Fenglin Niu, and Aibing Li. 2009. “Upper Mantle Structure beneath the Caribbean-South American Plate Boundary from Surface Wave Tomography.” *Journal of Geophysical Research* 114 (B1). https://doi.org/10.1029/2007jb005507.

Pasyanos, Michael E., T. Guy Masters, Gabi Laske, and Zhitu Ma. 2014. “LITHO1.0: An Updated Crust and Lithospheric Model of the Earth.” *Journal of Geophysical Research, [Solid Earth]* 119 (3): 2153–73.

Turcotte, Donald, and Gerald Schubert. 2014. *Geodynamics*. Cambridge University Press.